Noninvasive imaging of tumors using temporal log-slope difference mappings

Zhixiong Guo[a*], Siew Kan Wan[a], David A. August[b,e], Jinpin Ying[c],
Stanley M. Dunn[d], and John L. Semmlow[d, e]
[a]M&AE Department, Rutgers University, 98 Brett Road, Piscataway, NJ 08854, USA;
[b]The Cancer Institute of New Jersey, New Brunswick, NJ 08903, USA;
[c]Bell Labs, Lucent Technologies, Holmdel, NJ 07733, USA;
[d]Dept. of Biomedical Engineering, Rutgers University, Piscataway, NJ 08854, USA;
[e]Dept. of Surgery, UMDNJ RWJ Medical School, New Brunswick, NJ 08901, USA

ABSTRACT

An optical temporal log-slope difference mapping approach is proposed for cancerous tumor detection; in which target tissues are illuminated by near-infrared ultrashort laser pulses, and backscattered time-resolved light signals are collected. By analyzing the log-slopes of the temporally decaying signals, a log-slope distribution on the detection surface is obtained. After administration of absorption contrast agents, the presence of cancerous tumors increases the decaying steepness of the transient signals. The mapping of log-slope difference between native tissue and absorption-enhanced cancerous tissue indicates the location and projection of tumors on the detection surface. In this paper, we examine this method in the detection of tumor inside a model tissue through Monte Carlo simulation. The tissue model has a spherical tumor of different sizes embedded at the tissue center. It is found that tumors with size not less than 4 mm in diameter in the tissue model can be accurately projected on the detection surface by the proposed log-slope difference mapping method. The image processing is very fast and does not require any inverse optimization in image reconstruction. Parametric studies are conducted to examine to the influences of absorption contrast, tumor size and depth.

Keywords: Optical biomedical imaging, cancer detection, temporal log-slope, absorption contrast agent, ultrafast laser

1. INTRODUCTION

Cancer is the second leading cause of death among Americans. The American Cancer Society estimated that, in 2002, about 1.3 million Americans received new diagnosis of cancer and about 550 thousand died from this disease[1]. Early diagnosis is thought to represent an important opportunity to reduce both the morbidity and mortality that result from cancer. X-rays are commonly utilized for cancer screening and diagnosis. Chest x-rays, computed tomography, and mammography are the most commonly used modalities, but these methods can be costly and induce radiation exposure. Therefore, a great need exists for new noninvasive methods that pose less safety concerns, are low cost, portable and can be made widely available to large segments of the population.

Optical imaging methods are excellent candidates to provide an alternative imaging modality. Near-infrared (NIR) optical imaging has become increasingly attractive in recent years because NIR radiation is non-ionizing and the approach can lead to devices that are very compact and cost-effective. Furthermore, optical imaging can provide not only structural information[2-9] and functional information[10-13], but also cellular and molecular information[14,15]. Wavelengths in the NIR range, especially between 700-900 nm are widely used in research for diffuse optical tomography (DOT) because this spectral window has the lowest overall tissue absorption. In other words, light in that range has a much greater penetration depth allowing deep imaging up to several centimeters[16,17]. This is sufficient for many potential clinical applications, such as breast cancer screening and diagnosis. In DOT techniques, the target tissue is illuminated by a NIR laser (either pulsed or continuous-wave). Measurements of light signals (in either time-domain or frequency-domain) around the tissue boundary are made and used to reconstruct tissue images of optical parameters. Diseases are detected and/or diagnosed based on the difference of optical properties between normal and diseased tissues.

The most challenging task in utilizing DOT is the fact that NIR light is highly scattered in human tissues[18]. Unlike X-ray and PET that depend on the ballistic transmitted component of radiation emission, optical imaging has to deal with highly diffused and back-scattered light during image reconstruction. For highly diffused NIR light in biological tissues, the temporal and/or spatial intensity response sensed by a detector is not only determined by the optical properties along a direct path between the source and detector, but also by the optical properties in large surrounding regions as described in random walk theory[19]. Therefore, the image reconstruction in DOT is a formidable inverse problem, in which the tissue optical properties from a given experimental setup and a given set of measurements are determined through an optimization process using predicted boundary measurements in forward modeling with pre-assumed optical tissue parameters. An inverse process may easily require dozens of and hundreds of times of forward modeling. Previously most forward modeling approaches use a simplified diffusion approximation[20]. Rigorous radiation transfer simulation[21] is more appropriate, however, because biological tissues are generally heterogeneous and may contain low-scattering and/or high-absorbing regions. Given the complexity of both the distribution of tissue optical properties and a forward model approach, an image reconstruction in a typical DOT may take several hours to several days even with the latest computation technology. Further, an inverse problem is generally ill-posed and may lead to divergent results.

A much faster method to detect tumors can be based on the relative absorption contrast between the cancerous tumors and surrounding normal tissues, rather than the solution of the distributions of tissue optical parameters. Some recent reports have shown that the NIR absorption in cancerous regions can be greatly enhanced by the addition of absorbing dyes that have close affinity to the tumor. For example, indocyanine green dyes were used by Chance et al.[13] and Sevick-Muraca et al.[4]. The strong absorption will have a greater attenuation effect on the light signals detected at the tissue surface, especially for detectors most closely located to the cancerous tumor. This will result in an increase of decaying steepness in the temporal light signals. By measuring the temporal slopes of the logarithmically decaying signals over all detection points, a log-slope distribution on the tissue surface is obtained. The area with large log-slope values may represent a projection of tumors. In this approach, the complicated inverse image reconstruction is avoided.

The feasibility of log-slope approach in detecting a highly absorbing inhomogeneity in turbid media has been recently demonstrated[22] both experimentally and through simulation using a tiny graphite inclusion inside a homogeneous tissue phantom. This method is designed to accommodate the requirements of an inexpensive and rapid screening tool to detect the presence of tumors in human body before performing a comprehensive tomographic scan or biopsy examination. It was motivated by several published studies[23-28] that investigated the laser pulse response of both transmitted and backscattered signals in turbid media. The research on time-resolved reflectance measurement can be retraced to the pioneering work of Chance et al.[23] and Patterson et al.[24], in which the optical properties of tissues were obtained from fitting the experimental data with a standard solution of the diffusion theory for a semi-infinite homogeneous medium. They used information like the measured time of maximum signal and the long-time, asymptotic log slope (ALS) of the reflected pulse. Brewster and Yamada[25] found that the ALS of a simulated signal in a homogeneous semi-infinite slab increases as the scattering albedo decreases and vice versa. Zaccanti et al.[26] showed a significant dependence between the scattering coefficient of a homogenous medium and the broadening of a laser pulse: this broadening also affected the steepness of the pulse's decaying slope. Recent studies by Guo and his coauthors[20,28] extended these transient laser pulse investigations to two- and three-dimensional non-homogeneous tissue phantoms. They observed variations in the temporal log-slope of the detected signals in the presence of a relatively high absorbing tumor in the tissue phantoms.

In the direct log-slope approach, however, there is a fuzzy boundary around the absorbing inhomogeneous area and the edge effect[22] (signals decay fast in detectors located near surface edge) on the detecting surface is very pronounced. Here we propose a modified version of log-slope approach, i.e., mapping of temporal log-slope difference on the detection surface between log-slope distributions before and after administration of absorption contrast agent. Such a subtraction operation will eliminate the edge effect and diminish the fuzzy boundary of images. In this paper, the feasibility of the temporal log-slope difference mapping approach for cancer detection is studied by simulating light propagation in two tissue phantoms implanted with spherical tumors and evaluating the light detected from a coincident laser source over a predefined grid on the tissue surface. The propagation of photons in the tissue phantoms is simulated via our 3-D transient Monte Carlo radiative transfer method[29,30]. We present a comprehensive description to the simulation model as well as the modified Monte Carlo treatment of light transport in tissues with the presence of tumor. This is followed by a discussion of the analysis techniques applied to the detected signals to construct 2-D log-slope difference mappings that lead to the detection of cancer. Following this discussion, the detected 2-D images of simulated tumors in the tissue model will be presented.

2. METHODOLOGY

The model consists of a homogeneous cuboidal tissue phantom embedded with a spherical tumor located at the center (Fig. 1). The tissue phantom dimension is $20 \times 20 \times 20$ mm^3. The spherical tumor has a diameter of 6 mm if it is not specified. The NIR optical properties of the tissue phantom have been assigned to mimic biologic tissue. We assume the reduced scattering and absorption coefficients of the tissue are 1.0 mm^{-1} and 0.005 mm^{-1}, respectively. These typical values are selected in line with the studies in the literature[3-7]. The refractive index for both the tissue phantoms and tumors in the models are assumed to be n = 1.4. Optical properties of living tissue vary with light wavelength and physiological functions. The measured optical properties for different individuals are also different. All these will tremendously complicate the clinical use of conventional DOT techniques. However, they do not practically influence the present imaging method because the present method is based on the detection of relative absorption change. The exact value of tissue optical properties and their variations in actual tissues are insignificant. Hence, we may assume a homogeneous profile for tissue optical properties when contrast agents are used. The difficulty in the treatment of the heterogeneity of tissue structure and properties is overcome in this imaging method.

After injection of absorbing dyes, the absorption coefficient in the cancerous tumor region is assumed to be 0.2 mm^{-1}, while it is 0.01 mm^{-1} in the healthy tissue region. This corresponds to an absorbing dye uptake ratio of 40:1. The absorption contrast between the absorption-enhanced tumor and the healthy tissue is therefore 20:1. The absorption coefficient of malignant cancerous tissue is greater than that of healthy tissue, because increased blood flow leads to higher concentration or accumulation of oxy- and deoxy-hemoglobin (two natural absorbing chromophores inside human body at NIR wavelengths). As compared with the significant absorption augmentation through absorbing dye administration, however, this natural absorption contrast between cancerous and healthy tissues is negligible.

The laser delivery and detection system is set up so that the incident laser and backscattered signal coincide with each other. Ultrafast laser pulses are set to be delivered across a circular area with an effective radius of 0.1 mm. The intensity distribution is assumed to be a Gaussian profile with its peak intensity located at the center of the circular area. The scanning grid for detection model consists of a 19×19 equally spaced mesh with a resolution of 1mm. Due to the symmetry of this detection model, only one-fourth of the scanning grid results are needed in simulation.

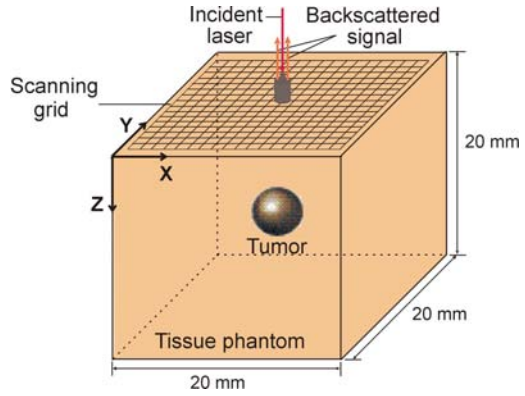

Figure 1 – Sketch of the detection model.

The simulation of experimental set-up including light illumination and signal measurements is executed using a Monte Carlo program adapted from Guo et al.[30]. Modifications have been made to the program code to consider the presence of tumors. The Monte Carlo simulation mimics photon propagation by calculating the random walks of a large number of photon bundles. Each emitted photon bundle begins from its initial position and time before making its way into the participating medium by a certain path length determined from statistical distribution and given by the equation:

$$l = -\frac{1}{\mu_e} \ln(\Re) \tag{1}$$

where μ_e represents the extinction coefficient of the medium and $\Re$ the random number generated by the computer. The photon bundle will experience scattering, absorption, or reflection at tissue-air interfaces before being detected. Fresnel

reflection[28] at the tissue-air boundary is considered because there is a significant refractive index mismatch between tissue and air. Total internal reflection occurs when the incoming angle is not less than the critical angle as determined by Snell's law. The energy attenuation due to absorption is calculated using the Beer-Lambert law:

$$I_{i+1} = I_i e^{-\mu_a l} \tag{2}$$

where I_i and I_{i+1} are photon bundle energy before and after each scattering event, respectively, l is the path length calculated from equation (1), and μ_a is the absorption coefficient of the medium along each scattering path length and varies depending on whether it is inside healthy tissue or inside the tumor. In the event where the photon bundle's path traverses both the normal tissue and tumor regions, the overall energy attenuation is calculated from two successive attenuations in the tissue and tumor regions, respectively. The first attenuation will be based on the distance to the tissue-tumor interface with the current extinction coefficient, while the second attenuation is based on the remaining path length with the extinction coefficient corresponding to the medium that the photon bundle is traveling towards. The remaining path length l_2 is calculated based on the conservation of optical depth and is given by:

$$l_2 = \frac{(\mu_{e1} l_0 - \mu_{e1} l_1)}{\mu_{e2}} \tag{3}$$

where l_0 corresponds to the path length of the originally intended travel distance calculated from Eq. (1), and l_1 corresponds to the distance to the tissue-tumor interface from the starting point. The constants μ_{e1} and μ_{e2} refer to the extinction coefficients of the medium before and after the tissue-tumor interface. In our simulation, we used a total of 10^8 photon bundles on each node of the scanning grid.

A single detecting point calculation takes about 2 hours on a DELL PC equipped with a 1.7GHz Pentium 4 processor and 256MB memory. The simulation on the top surface of the tissue phantom requires 361 runs for detection model with a 19 x 19 scanning grid. Since the calculation task is too heavy for a single PC, the final calculations were conducted in a 64-CPU workstation cluster. It must be pointed out that the above-mentioned computational effort was for simulating an experimental setup to obtain a "simulated" measurement. It is not used for image processing and reconstruction. If a practical experiment is set up, real measurement can be completed in minutes, and the previous simulation process is not necessary.

Due to the high-scattering and low-absorption of NIR light in tissues, detected signal pulses at the boundary will be broadened considerably. At the decaying part of the signal, there exists an asymptotic log-slope region that is sensitive to the distribution of absorption coefficients inside the tissue phantom. From our experience, the log-slope is best chosen in the time range of 300-700 ps. Prior to 300 ps the logarithmic signal is non-linear, while after 700 ps the signal strength is weak and the signal is strongly affected by a large zone beyond the optical axis. In order to form a 2-D mapping of log-slope difference to detect the tumor's projection onto the tissue surface, we first evaluate the log-slope distribution before the administration of absorbing contrast agent. This evaluation is followed by evaluation of the log-slope distribution after absorption enhancement. Then, a 2-D mapping of log-slope difference between these two log-slope distributions can be constructed. Due to the affinity of absorbing contrast agent for cancerous regions, the log-slope difference is significantly larger in the tumor region than in other regions. This mechanism is illustrated in Fig. 2 which shows log-slope profiles versus x-position plotted along y = 10 mm in three different cases: before absorption enhancement, after absorption enhancement, and the net difference between the previous two profiles. For each detection surface, we obtained two sets of log-slope distributions corresponding to the cases before and after the addition of contrast agent, respectively. By proceeding with the log-slope subtraction process, a log-slope difference mapping was constructed. In the cancerous region, the difference is large. A final filtering process was applied to highlight the image contrast and to suppress unwanted noise. Values below a pre-assigned cut-off filter level were removed. The computation in image processing and mapping construction took between two to three minutes.

3. RESULTS AND DISCUSSION

The complete log-slope mappings are presented in Figs. 3 and 4. Figure 3a shows the log-slope mapping on a surface of the cuboidal tissue phantom before administration of absorbing contrast agent. The log-slope values range from –5.60 to –8.80. The presence of tumor is not immediately identifiable due to the strong edge effect associated with the relatively

small geometry in this detection model. Figure 3b shows the result after absorption enhancement. The log-slope values range from –6.20 to –9.20. The absolute values of the log-slopes increase. This indicates that the decay of the log-slope signal has become steeper since more energy is absorbed by the absorption-enhanced tumor.

Figure 4a was obtained by subtracting the log-slopes in Fig. 3b from the corresponding values in Fig. 3a. The initial subtraction created log-slope difference values that fell between 0.05 and 0.53 for the whole 2-D distribution. A larger difference value indicates stronger absorption augmentation in the cancerous region. In this simulation result, the majority of the higher values (above 0.42) were concentrated on the region where the tumor is located. The presence of tumor at the center in Fig. 4a is clearly visible. Figures 4b, 4c, and 4d show images of the tumor projection on the detection surface after applying various filters to the image in Fig. 4a. The cut-off filter[25] value is 60% of the peak log-slope difference value in Fig. 4b, 70% in Fig. 4c, and 80% in Fig. 4d, respectively. As the cut-off filter value increased, the effective imaging area representing the tumor projection decreased accordingly. A 70% cut-off filter level was found to produce images clear enough for visualizing the tumor projection (indicated by the white circle in the figures). A more general and effective cut-off filter value can be established when more cases are simulated and analyzed. Although the filtered log-slope difference image corresponds well to the shape and location of the actual tumor, the image boundary does not resemble a perfect circle. The main reason is due to the limited resolution of the scanning grid defined in the simulation model. Further increase in resolution should result in a better image quality.

It is necessary to perform several parametric studies to investigate the potential of this method under different conditions. Firstly, the tumor may be located close to the skin surface or deep inside the tissue. The spherical tumor's depth has been set to be 4 mm (see Fig. 5), 7 mm (see Fig. 6), 10 mm (see Fig. 4), 13 mm (see Fig. 7) and 16 mm (see Fig. 8) below the detection surface while the optical properties and tumor size are kept at 0.20 mm^{-1} and 6 mm, respectively. At shallow depth, the presence of tumor is clearly visible because its absorption contrast is significantly higher than the surrounding region. As tumor depth increases, the log-slope difference in tumor region starts to diminish and soon blend in with the background. Based on the results, the presence of tumor is still identifiable at 13 mm deep due to large concentration of high lop-slope difference. However, the presence of tumor cannot be clearly seen at 16 mm in which the log-slope difference is slight.

Next parametric study deals with the absorption coefficient change in tumor. This study is important because the concentration of absorption dye may vary. Figures 9 through 12 show the log-slope difference mappings for tumor with absorption coefficient of 0.10 mm^{-1}, 0.25 mm^{-1}, 0.30 mm^{-1} and 0.35 mm^{-1}, respectively. The tumor's depth and size are 10 mm and 6 mm, respectively. The case with absorption coefficient of 0.20 mm^{-1} has been discussed in Fig. 4. In general, the magnitude of log-slope difference mapping is proportional to the tumor's absorption coefficient. It is found that the contrast from a tumor with absorption coefficient of 0.10 mm^{-1} is insufficient to be accurately diagnosed when embedded 10 mm deep inside bulk tissue with background absorption coefficient of 0.01 mm^{-1}. However, for cases where tumor's absorption coefficient is not less than 0.20 mm^{-1}, the presence of tumor can be easily detected.

The parametric study on tumor's diameter is also performed to investigate the limit of this optical technique in detecting early stage breast tumors. The log-slope difference mappings for tumor with diameter of 2 mm, 4 mm, 8 mm and 10 mm are investigated and shown in Figs. 13 through 16, respectively. The tumor's depth and absorption coefficient are 10 mm and 0.20 mm^{-1}, respectively. In Fig. 13, the contrast from a 2 mm spherical tumor at 10 mm deep is too weak to be clearly identified. However, for all other cases where tumor's diameter is not less than 4 mm, the presence of tumor can be easily detected.

4. CONCLUSIONS

This study evaluated a novel tumor detection method based on NIR log-slope difference mapping. The feasibility of this approach as a quick yet accurate preliminary diagnostic tool for early cancer detection was demonstrated numerically. The temporal log-slope difference between tissues before and after absorption enhancement was shown to be very large for those detection points directly above the embedded tumor. The results in the example detection model accurately showed the shape and location of the embedded tumors. The proposed temporal log-slope difference mapping method is capable of forming 2-D tumor projection for the detection of cancerous tumors. The images were directly constructed. The image processing and construction took only a couple of minutes in a PC. The present imaging method does not require any inverse image reconstruction. These features will greatly enhance the clinical utility of the present method. Parametric studies show that a 6 mm diameter tumor embedded up to 13 mm below the surface can be detected. The

study also suggested that the absorption contrast ratio between a tumor of 6 mm in diameter at 10 mm depth and its surrounding tissue should be about 20:1 or higher in order to produce highly visible image of the tumor. Tumor as small as 4 mm in diameter at 10 mm can also be imaged using the proposed log-slope difference mapping method.

5. ACKNOWLEDGMENTS

Z. Guo acknowledges the partial support of this research from the New Jersey Space Grant Consortium, the Academic Excellence Fund award from Rutgers University, and the NSF grant (CTS-0318001).

6. REFERENCES

1. American Cancer Society, "Cancer Facts & Figures 2003". http://www.cancer.org/downloads/STT/CAFF2003PWSecured.pdf
2. B. Tromberg, A. Yodh, E. Sevick-Muraca and D. Pine, "Diffusing photons in turbid media: introduction to the feature," *Appl. Opt.*, **36**, 9-231 (1997).
3. M.J. Holboke, B.J. Tromberg, X. Li, N. Shah, J. Fishkin, D. Kidney, J. Butler, B. Chance and A. G. Yodh, "Three-dimensional diffuse optical mammography with ultrasound localization in a human subject," *J. Biomedical Optics*, **5**, 237-247 (2000).
4. R. Roy, A. Godavarty, E. M. Sevick-Muraca, "Fluorescence-enhanced optical tomography using referenced measurements of heterogeneous media," IEEE Transactions on Medical Imaging, 22, 824-836 (2003).
5. J.C. Hebden, H. Veenstra, H. Dehghani, E. M. C. Hillman, M. Schweiger, S. R. Arridge, and D. T. Delpy, "Three dimensional time-resolved optical tomography of a conical breast phantom," *Appl. Opt.*, **40**, 3278-3287 (2001).
6. J.P. Culver, R. Choe, M. J. Holboke, L. Zubkov, T. Durduran, A. Slemp, V. Ntziachristos, B. Chance, and A. G. Yodh, "Three-dimensional diffuse optical tomography in the parallel plane transmission geometry: Evaluation of a hybrid frequency domain/continuous wave clinical system for breast imaging," *Med. Phys.*, **30**, 235-247 (2003).
7. B.W. Pogue, S. Geimer, T.O. McBride, S. D. Jiang, U. L. Osterberg and K. D. Paulsen, "Three-dimensional simulation of near-infrared diffusion in tissue: boundary condition and geometry analysis for finite-element image reconstruction," *Appl. Opt.*, **40**, 588-600 (2001).
8. M. A. Bartlett and H.B. Jiang, "Effect of refractive index on the measurement of optical properties in turbid media," *Appl. Opt.*, **40**, 1735-1741 (2001).
9. J. Wu, L. Perelman, R. R. Dasari, and M. S., Feld, "Fluorescence tomographic imaging in turbid media using early-arriving photons and Laplace transporms", *PNAS*, **94**, 8783-8788 (1997).
10. D.A. Benaron, S.R. Hintz, A. Villringer, D. Boas, A. Kleinschmidt, J. Frahm, C. Hirth, H. Obrig, J.C. van Houten, E. L. Kermit, W. F. Cheong and D. K. Stevenson, "Noninvasive functional imaging of human brain using light," *J. Cereb. Blood Flow Metab.*, **20**, 469-477 (2000).
11. B.J. Tromberg, N. Shah, R. Lanning, A. Cerussi, J. Espinoza, T.Pham, L. Svaasand and J. Butler, "Non-invasive in vivo characterization of breast tumor using photon migration spectroscopy," *Neoplasia*, **2**, 1-15 (2000).
12. D.A. Boas, G. Strangman, J.P. Culver, R.D. Hoge, G. Jasdzewski, R. A. Poldrack, B. R. Rosen and J. B. Mandeville, "Can the cerebral metabolic rate of oxygen be estimated with nearinfrared spectroscopy?," *Phys. Med. Biol.*, **48**, 2405-2418 (2003).
13. V. Ntziachristos, A. G. Yodh, M. Schnall and B. Chance, "Concurrent MRI and diffuse optical tomography of breast after indocyanine green enhancement," *PNAS*, **97**, 2767-2772 (2000).
14. E. Betzig, "Proposed method for molecular optical imaging," *Opt. Let.*, **20**, 237-239 (1995).
15. R. Weissleder, C.H. Tung, U. Mahmood and A. Bogdanov Jr., "In vivo imaging of tumor with protease-activated near-infrared fluorescent probes," *Nature Biotech.*, **17**, 375-378 (1999).
16. C.L. Smithpeter, A.K. Dunn, A.J. Welch and R. Richard-Kortum, "Penetration depth limits of in vivo confocal reflectance imaging," *Appl. Opt.*, **37**, 2749-2754 (1998).
17. L. Reinisch, "Laser physics and tissue interactions," *Otolaryngologic Clinics of North America*, **29**, 893-914 (1996).
18. B. Tromberg, A. Yodh, E. Sevick-Muraca and D. Pine, "Diffusing photons in turbid media: introduction to the feature," *Appl. Opt.*, **36**, 9 (1997).
19. L. Florescu and S. John, "Theory of photon statistics and optical coherence in a multiple-scattering random-laser medium," *Physical Review E*, **69**(4), 1-16 (2004).

20. Z. Guo, S. K. Wan, K. H. Kim and C. Kosaruja, "Comparing Diffusion Approximation with Radiation Transfer Analysis for Light Transport in Tissues," *Optical Review*, **10** (5), 415-421 (2003).
21. Z. Guo and Kumar, "Discrete Ordinates Solution of Short Pulse Laser Transport in Two-Dimensional Turbid Media," *Appl. Opt.*, **40**(19), 3156-3163 (2001).
22. S. K. Wan, Z. Guo, S. Kumar, J. Aber and B. A. Garetz, "Noninvasive detection of inhomogeneity in turbid media time-resolved log-slop analysis," *J. Quantitative Spectroscopy & Radiative Transfer*, **84** (4), 493-500 (2004).
23. B. Chance, S. Nioka, J. Kent, K. McCully, M. Fountain, R. Greenfeld and G. Holtom, "Time-resolved spectroscopy of hemoglobin and myoglobin in resting and ischemic muscle", *Anal. Biochem.*, **174**, 698-707 (1988).
24. M.S. Patterson, B. Chance and B.C. Wilson, "Time-resolved reflectance and transmittance for the noninvasive measurement of tissue optical properties," *Appl. Opt.*, **28**, 2331-2336 (1989)
25. M. Q. Brewster and Y. Yamada, "Optical properties thick, turbid media from picosecond time resolved light scattering measurements," *Int. J. Heat Mass Transfer*, **38**, 2569-2581 (1995).
26. G. Zaccanti, P. Bruscaglioni, A. Ismaelli, L. Carraresi, M. Gurioli and Q. Wei, "Transmission of a pulse thin light beam through thick turbid media: experimental results," *Appl. Opt.*, **31**, 2141-2147 (1992).
27. F. Liu, K. M. Yoo and R. R. Alfano, "Ultrafast laser-pulse transmission and imaging through biological tissues," *Appl. Opt.*, **32**(4), 554-558 (1993).
28. Z. Guo and K. H. Kim, "Ultrafast Laser Radiation Transfer in Heterogeneous Tissues Using Discrete Ordinates Method," *Appl. Opt.*, **42**(16), 2897-2905 (2003).
29. Z. Guo, S. Kumar and K. C. San, "Multidimensional Monte Carlo simulation of short-pulse laser transport in scattering media," *J. Thermophysics Heat Transfer*, **14**(4), 504-511 (2000).
30. Z. Guo, J. Aber, B. Garetz and S. Kumar, "Monte Carlo Simulation and Experiments of Pulsed Radiative Transfer," *J. Quantitative Spectroscopy & Radiative Transfer*, **73**, 159-168 (2002).

* guo@jove.rutgers.edu; phone 1 732 445-2024; fax 1 732 445-3124

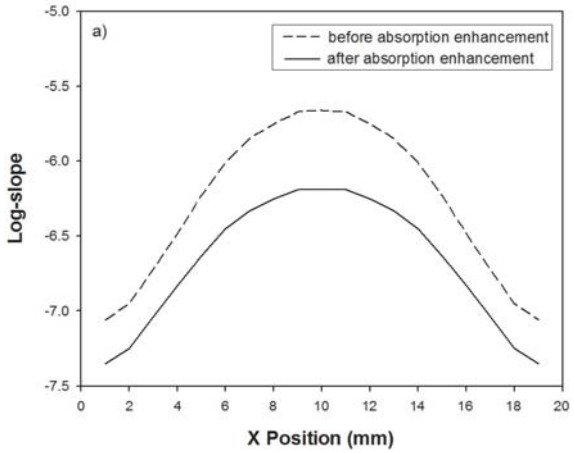

Figure 2a – Plots of log-slope versus x-position along y = 10 mm

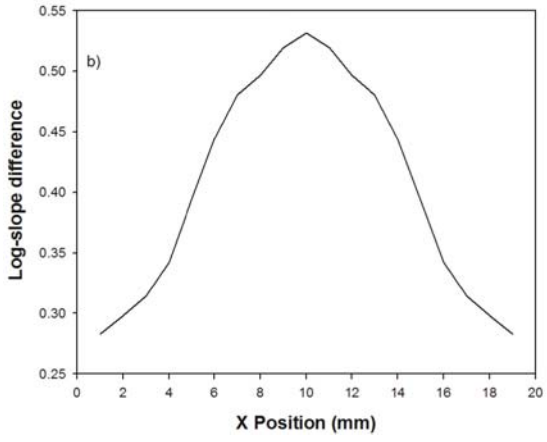

Figure 2b – Profile of log-slope difference before and after absorption enhancement.

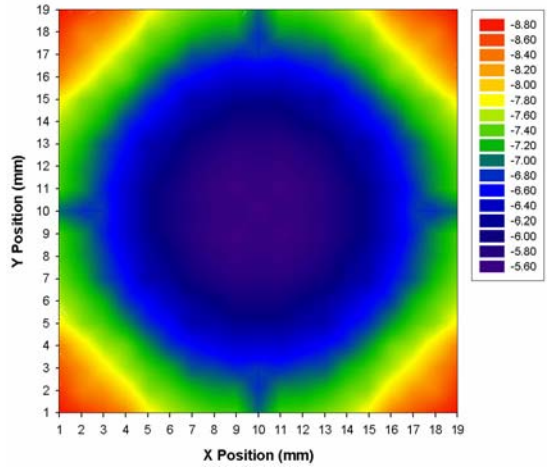

Figure 3a – Log-slope mapping results before administration of contrast agent.

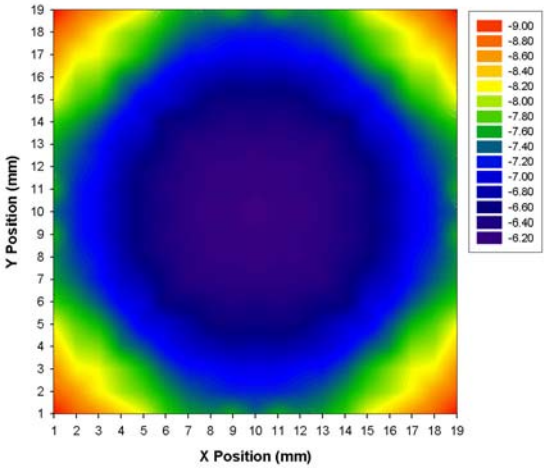

Figure 3b – Log-slope mapping results after administration of absorption contrast agent.

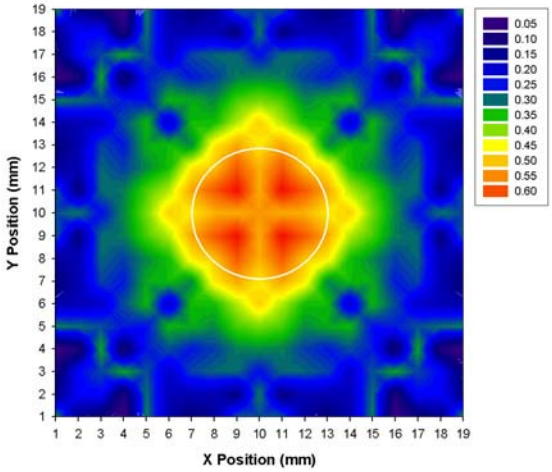

Figure 4a – Mapping of log-slope difference between log-slope distributions before and after absorption enhancement.

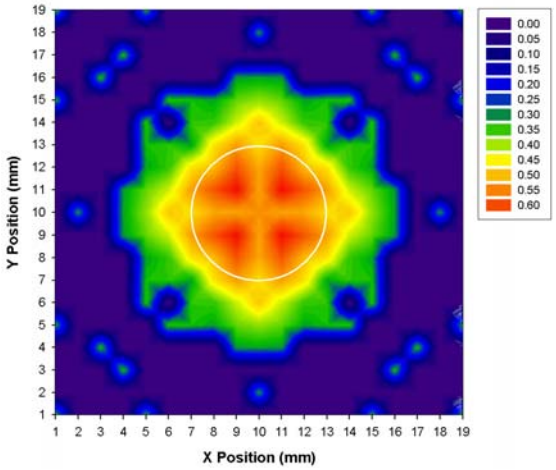

Figure 4b – Mapping of log-slope difference with 60% cut-off filter.

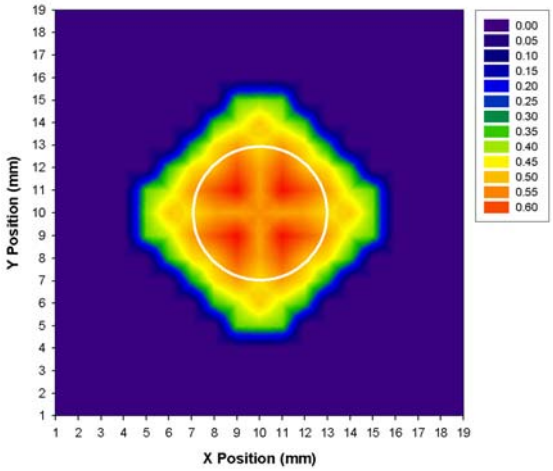

Figure 4c – Mapping of log-slope difference with 70% cut-off filter.

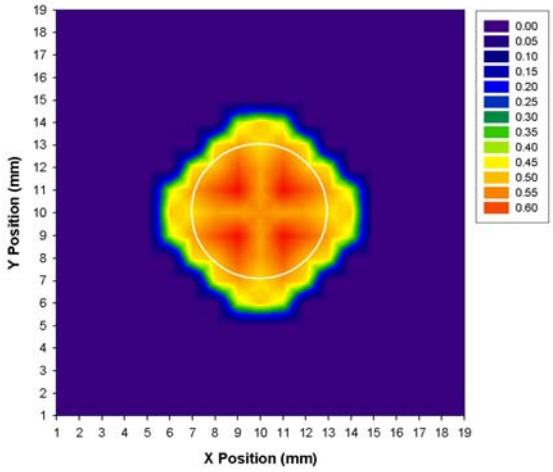

Figure 4d – Mapping of log-slope difference with 80% cut-off filter.

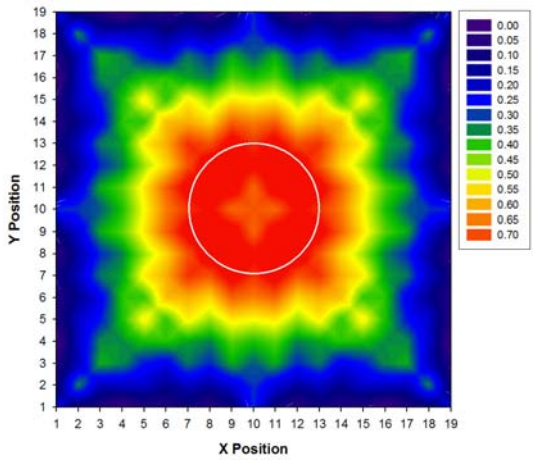

Figure 5a – Mapping of log-slope difference for tumor at 4 mm deep.

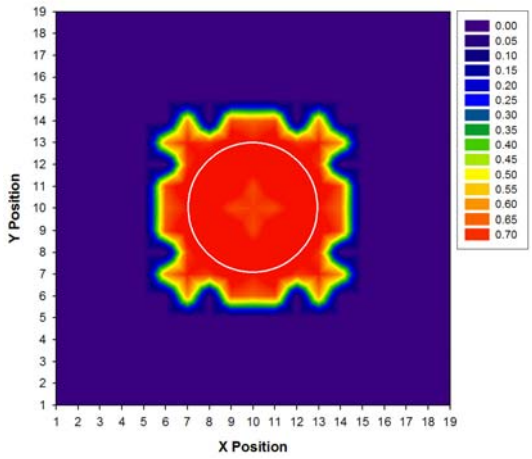

Figure 5b – Mapping of log-slope difference for tumor at 4 mm deep after 70% cut-off filter.

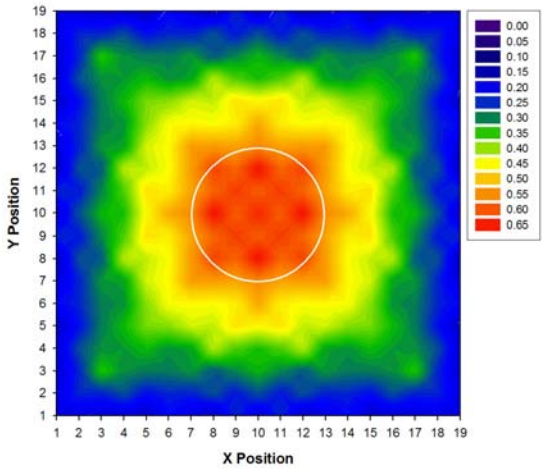

Figure 6a – Mapping of log-slope difference for tumor at 7 mm deep.

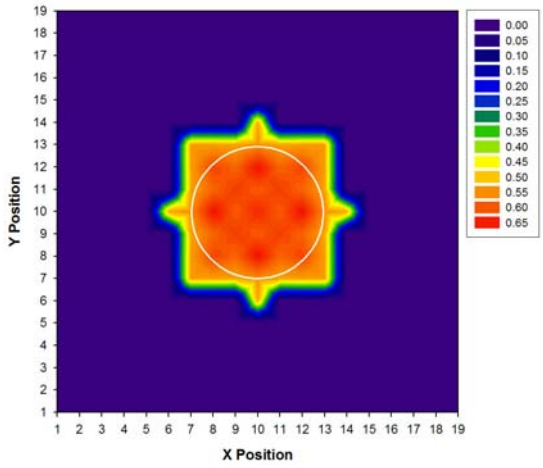

Figure 6b – Mapping of log-slope difference for tumor at 7 mm deep after 70% cut-off filter.

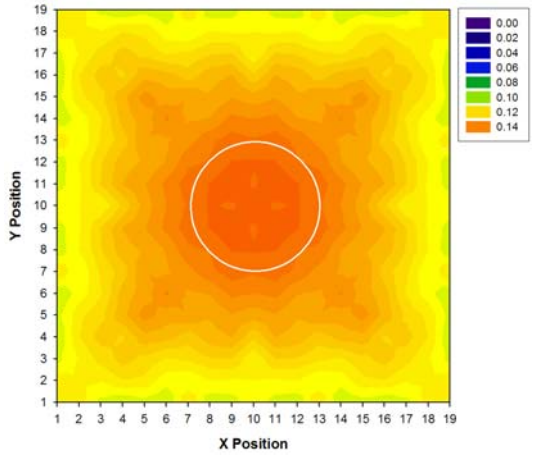

Figure 7a – Mapping of log-slope difference for tumor at 13 mm deep.

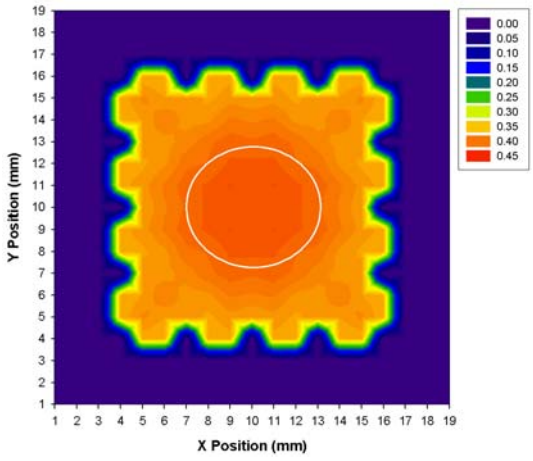

Figure 7b – Mapping of log-slope difference for tumor at 13 mm deep after 70% cut-off filter.

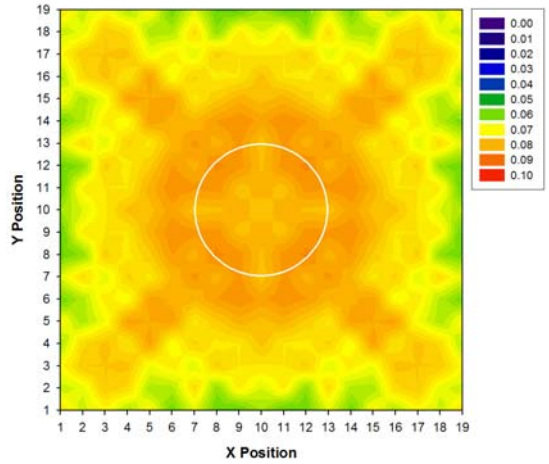

Figure 8a – Mapping of log-slope difference for tumor at 16 mm deep.

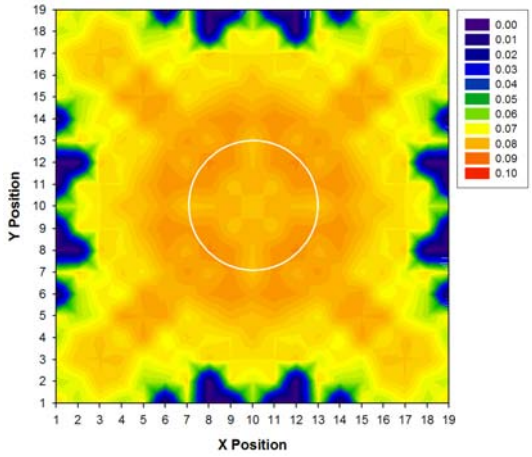

Figure 8b – Mapping of log-slope difference for tumor at 16 mm deep.

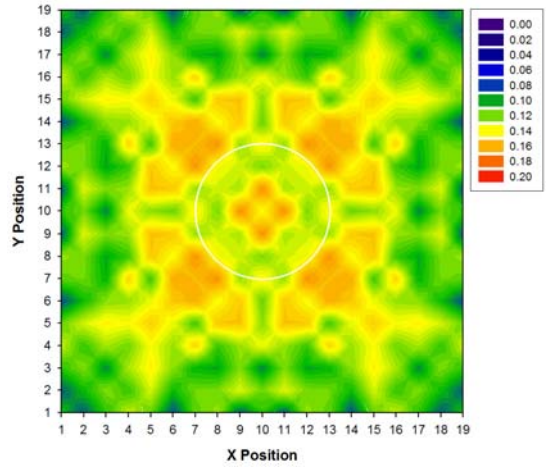

Figure 9a – Mapping of log-slope difference for tumor with absorption coefficient of 0.10 mm^{-1}.

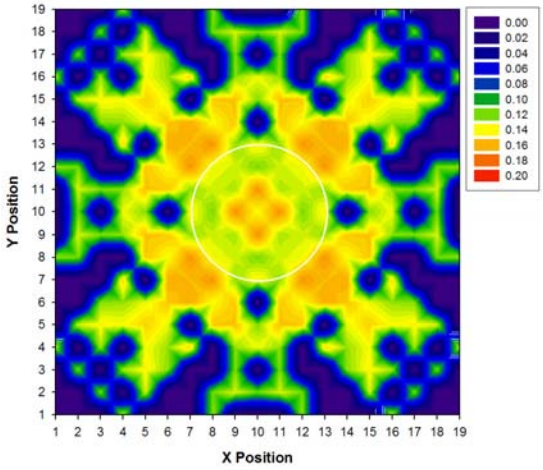

Figure 9b – Mapping of log-slope difference for tumor with absorption coefficient of 0.10 mm^{-1} after 70% cut-off filter.

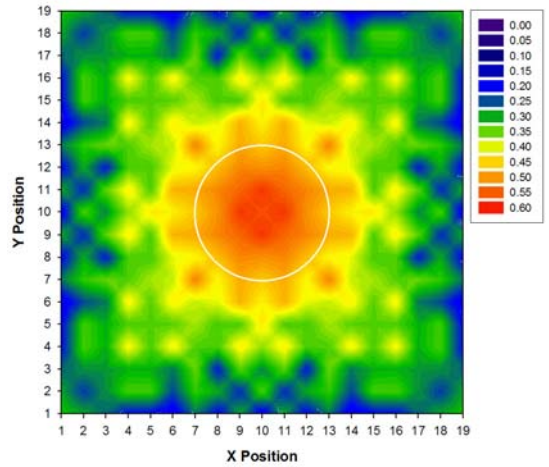

Figure 10a – Mapping of log-slope difference for tumor with absorption coefficient of 0.25 mm^{-1}.

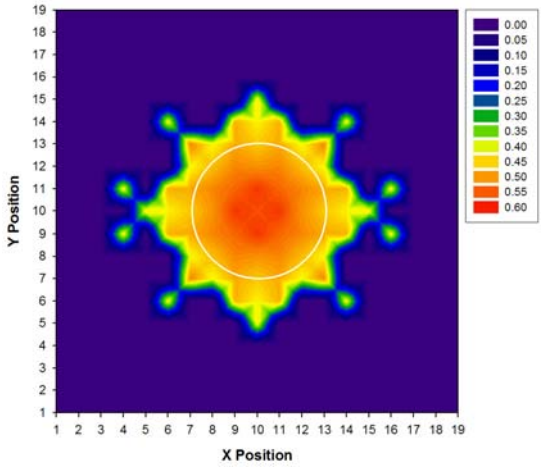

Figure 10b – Mapping of log-slope difference for tumor with absorption coefficient of 0.25 mm^{-1} after 70% cut-off filter.

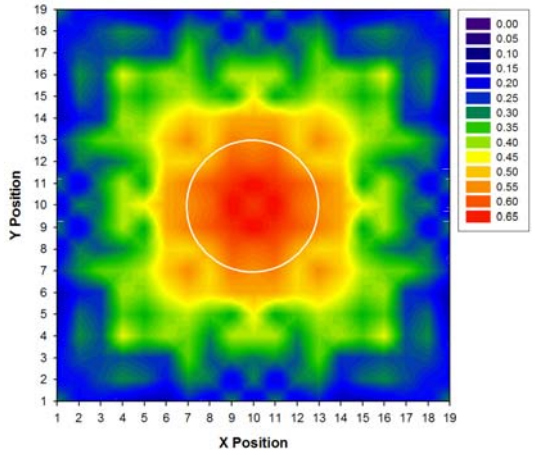

Figure 11a – Mapping of log-slope difference for tumor with absorption coefficient of 0.30 mm^{-1}.

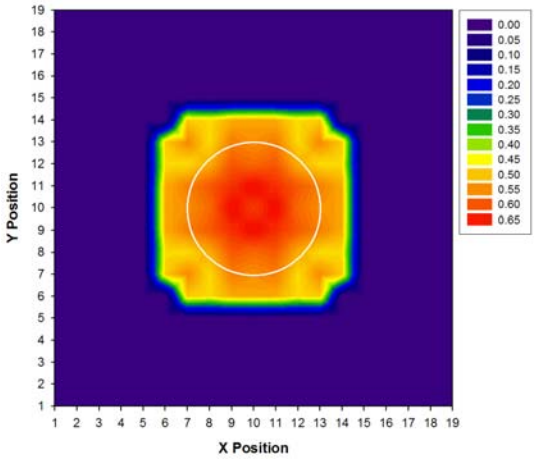

Figure 11b – Mapping of log-slope difference for tumor with absorption coefficient of 0.30 mm^{-1} after 70% cut-off filter.

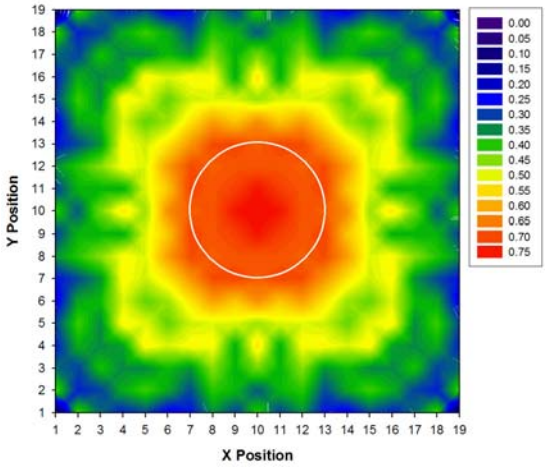

Figure 12a – Mapping of log-slope difference for tumor with absorption coefficient of 0.35 mm^{-1}.

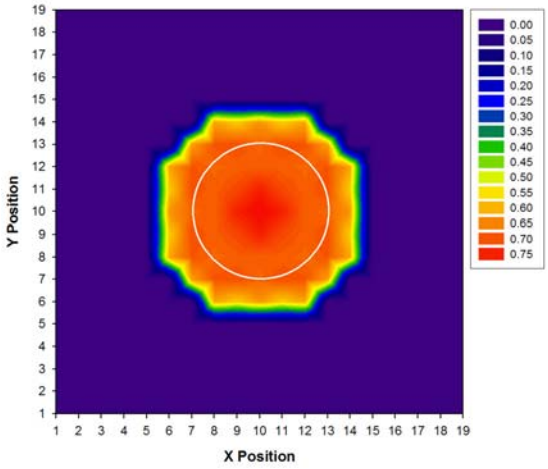

Figure 12b – Mapping of log-slope difference for tumor with absorption coefficient of 0.35 mm^{-1} after 70% cut-off filter.

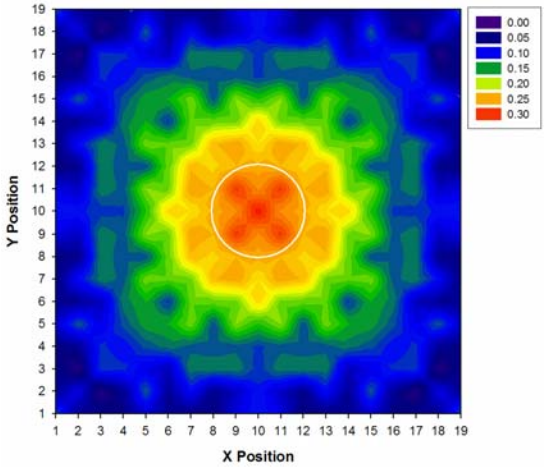

Figure 13a – Mapping of log-slope difference for tumor of 2 mm diameter.

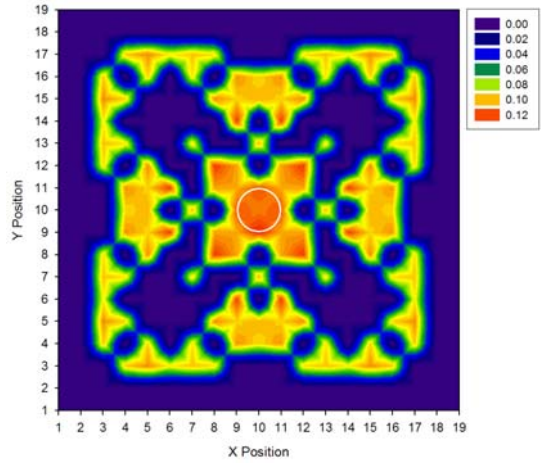

Figure 13b – Mapping of log-slope difference for tumor of 2 mm diameter after 70% cut-off filter.

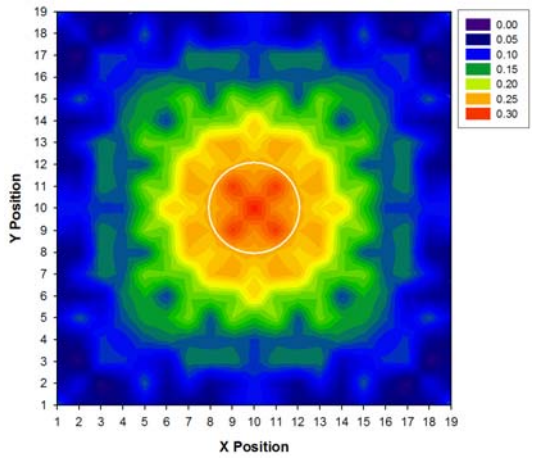

Figure 14a – Mapping of log-slope difference for tumor of 4 mm diameter.

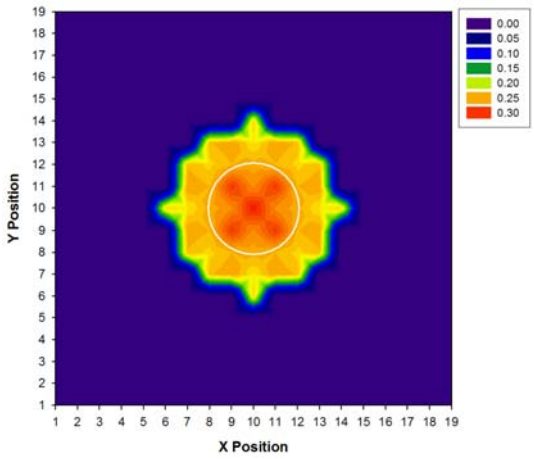

Figure 14b – Mapping of log-slope difference for tumor of 4 mm diameter after 70% cut-off filter.

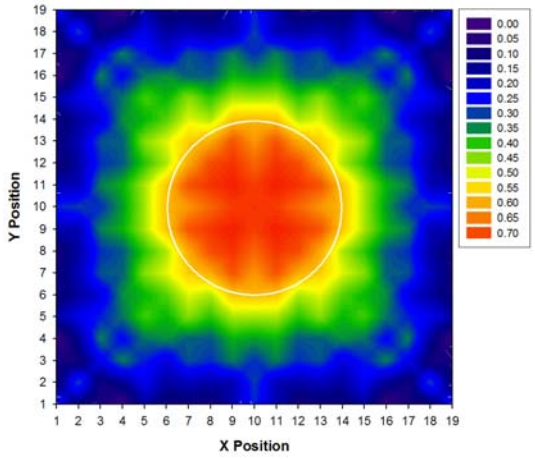

Figure 15a – Mapping of log-slope difference for tumor of 8 mm diameter.

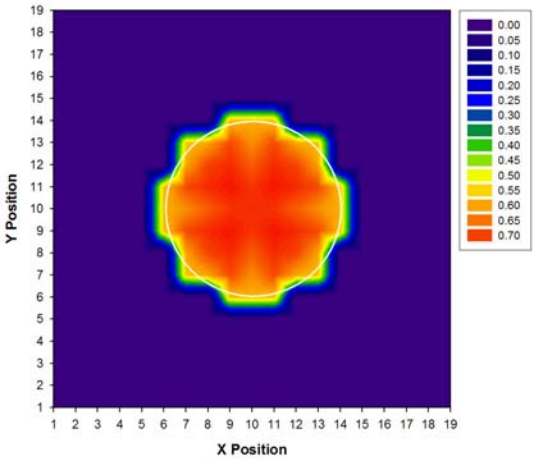

Figure 15b – Mapping of log-slope difference for tumor of 8 mm diameter after 70% cut-off filter.

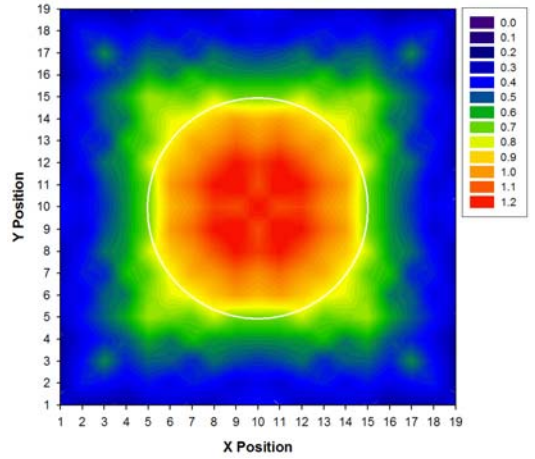

Figure 16a – Mapping of log-slope difference for tumor of 10 mm diameter.

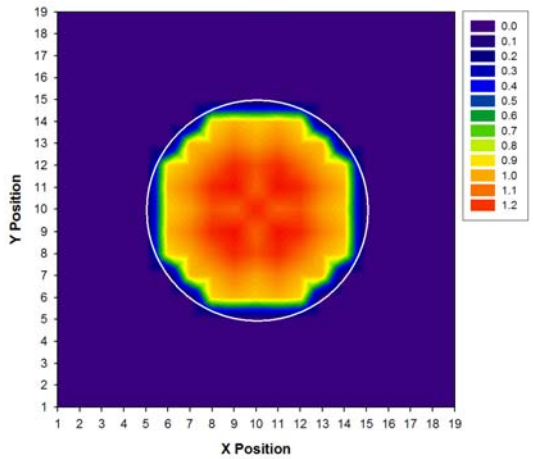

Figure 16b – Mapping of log-slope difference for tumor of 10 mm diameter after 70% cut-off filter.